



PAPER

OPEN ACCESS

RECEIVED

23 December 2021

REVISED

1 June 2022

ACCEPTED FOR PUBLICATION

10 June 2022

PUBLISHED

27 June 2022

Original content from this work may be used under the terms of the [Creative Commons Attribution 4.0 licence](#).

Any further distribution of this work must maintain attribution to the author(s) and the title of the work, journal citation and DOI.



Direct measurement of oxygen reduction reactions at neurostimulation electrodes

Jiří Ehlich^{1,4} , Ludovico Migliaccio^{1,4} , Ihor Sahalianov¹ , Marta Nikić^{1,2} , Jan Brodský¹ , Imrich Gablech¹ , Xuan Thang Vu³ , Sven Ingebrandt³ and Eric Daniel Glowacki^{1,*}

¹ Bioelectronics Materials and Devices Laboratory, Central European Institute of Technology CEITEC, Brno University of Technology, Purkyňova 123, 61200 Brno, Czech Republic

² Institute of Neuroelectronics, Technical University of Munich, Munich, Germany

³ Institute of Materials in Electrical Engineering 1, RWTH Aachen University, 52074 Aachen, Germany

⁴ These authors are contributed equally.

* Author to whom any correspondence should be addressed.

E-mail: eric.daniel.glowacki@ceitec.vutbr.cz

Keywords: bioelectronics, neurostimulation, faradaic reactions, hypoxia, reactive oxygen species

Supplementary material for this article is available [online](#)

Abstract

Objective. Electric stimulation delivered by implantable electrodes is a key component of neural engineering. While factors affecting long-term stability, safety, and biocompatibility are a topic of continuous investigation, a widely-accepted principle is that charge injection should be reversible, with no net electrochemical products forming. We want to evaluate oxygen reduction reactions (ORR) occurring at different electrode materials when using established materials and stimulation protocols. **Approach.** As stimulation electrodes, we have tested platinum, gold, tungsten, nichrome, iridium oxide, titanium, titanium nitride, and poly(3,4-ethylenedioxythiophene):poly(styrene sulfonate). We use cyclic voltammetry and voltage-step amperometry in oxygenated versus inert conditions to establish at which potentials ORR occurs, and the magnitudes of diffusion-limited ORR currents. We also benchmark the areal capacitance of each electrode material. We use amperometric probes (Clark-type electrodes) to quantify the O₂ and H₂O₂ concentrations in the vicinity of the electrode surface. O₂ and H₂O₂ concentrations are measured while applying DC current, or various biphasic charge-balanced pulses of amplitude in the range 10–30 μC cm⁻²/phase. To corroborate experimental measurements, we employ finite element modelling to recreate 3D gradients of O₂ and H₂O₂. **Main results.** All electrode materials support ORR and can create hypoxic conditions near the electrode surface. We find that electrode materials differ significantly in their onset potentials for ORR, and in the extent to which they produce H₂O₂ as a by-product. A key result is that typical charge-balanced biphasic pulse protocols do lead to irreversible ORR. Some electrodes induce severely hypoxic conditions, others additionally produce an accumulation of hydrogen peroxide into the mM range. **Significance.** Our findings highlight faradaic ORR as a critical consideration for neural interface devices and show that the established biphasic/charge-balanced approach does not prevent irreversible changes in O₂ concentrations. Hypoxia and H₂O₂ can result in different (electro)physiological consequences.

1. Introduction

Electrical neurostimulation is an established part of numerous implantable bioelectronics devices like deep brain stimulators [1], peripheral nerve stimulation devices [2], spinal cord stimulators [3], and retinal prosthetics [4, 5]. Electrical stimulation involves

charge injection from an electrode surface into physiological electrolyte. The safety and reliability of this process is a vital consideration. Mechanisms of charge exchange at the electrode/electrolyte interface are the subject of extensive research, and can be divided into capacitive, pseudo-capacitive, and faradaic [6–8]. Capacitive charge injection

involves the charging and discharging of electrolytic double-layers, and no charge is transferred to species in solution. The pseudo-capacitive mechanism, also known as pseudo-faradaic, features redox reactions of the electrode material itself. These reactions can result in high density of charge transfer, and this transfer can be highly reversible. The third category is faradaic, where charge is transferred to a species in solution via a redox process occurring at the electrode/electrolyte interface. This process may or may not be reversible, depending on kinetic factors like activation barriers (*aka* overpotentials) for a given reaction as well as diffusion of reactants/products. A stimulation electrode works by injecting current into a physiological medium and the resultant electric fields modulate the membrane potential of nearby excitable cells. For instance, a cathodic pulse will efficiently depolarize cell membranes and activate voltage-gated sodium channels, triggering action potentials. Cathodic, i.e. negative currents, have been long recognized as being most efficient at eliciting action potentials. However, it follows that charge artificially injected into a physiological environment should be subsequently removed, that is no net charging of the system should occur. This is because net charge remaining would correspond to polarization of the electrode, or to electrochemical changes in the biological surrounding itself. These changes could potentially be toxic or otherwise spurious. For this reason, virtually all neurostimulation protocols for both basic research and implanted biomedical devices rely on biphasic operation [6]. Charge-balanced, cathodic-leading pulses are the standard [9]. This way, the total injected cathodic charge in the first phase is equalized by an equal-charge anodic phase. In principle, any electrochemical reaction products formed on the electrode during the leading phase should be reoxidized during the second, anodic, phase [7, 10]. Determining safe limits for charge injection is the topic of debate and several empirical norms have been suggested for various *in vivo* applications. A number of studies have considered the reversibility of faradaic electrochemistry during biphasic pulsing [11]. Nearly all of these studies focus on testing corrosion of the metal electrode itself, or voltage excursions beyond the water-splitting window, and thus hydrogen evolution or oxygen evolution reactions [7, 11, 12]. The possibility of oxygen reduction, occurring during the cathodic stimulation phase, has received relatively little attention [13, 14], despite the fact that thermodynamically it is much more favoured than hydrogen evolution (by at least 1.23 V). Oxygen is present in all physiological fluids. While it is transported in heme-bound form in the vasculature, in excitable neural tissues, oxygen travels through the extracellular and intracellular space by passive diffusion. Neural tissue oxygenation levels vary depending on species, anaesthesia, location. The highest possible

equilibrium concentration of dissolved O₂ is about 250 μM. This is the same level of oxygenation as what is expected for a container of water open to ambient 21% atmospheric oxygen. This condition also applies for most *in vitro* experiments. We therefore perform this study with this 21% reference point, since it applies to *in vitro* conditions and with respect to *in vivo* this assumption mirrors the ‘best case’ scenario.

To our knowledge, there are four published studies which consider oxygen reduction reactions (ORR) on neurostimulation electrodes, primarily on Pt and Au [13–16]. These all rely on some form of transient electrochemical measurement techniques to estimate irreversible charge transfer to O₂, and all these studies agree that a substantial fraction of cathodic current can be irreversibly transferred to oxygen (reported ranges between 5% and 80%). None of these studies quantified the generation of peroxide via two-electron reduction, or actual oxygen concentration changes. In contrast to these works, we have designed our study to probe both O₂ and H₂O₂ concentrations in the vicinity of the electrode surface to quantify the effects of ORR directly, and have used the same technique to compare eight different neurostimulation electrode materials we have prepared in thin-film from: Ti, TiN, Au, IrO_x, Pt, W, NiCr, and poly(3,4-ethylenedioxythiophene):poly(styrene sulfonate), shortened as PEDOT:PSS. This list is chosen it represents common electrode materials used in both neuroscience/electrophysiology research as well as biomedical devices. In addition, a sample of commercial high-surface area TiN was tested [17]. This way, we can establish to what extent irreversible ORR can occur at neurostimulation electrodes, and compare and contrast different electrode materials. To corroborate experimentally-measured O₂ and H₂O₂ concentrations, we have also established finite element simulations to understand the geometry of concentration gradients over time.

2. Materials and methods

2.1. Model stimulation electrode preparation

Microscope slides (3 × 1) inch² were cleaned according to established methods, treated with oxygen plasma, and then sputter coated with a 100 nm layer of Ti using a Kaufman ion-beam source (IBS). The Ti acts as the common conducting layer below all studied samples, as it has excellent adhesion on glass and is a suitable underlayer for all the studied materials. Platinum (60 nm) is deposited using DC magnetron sputtering. W (60 nm) was deposited using the same sputtering system. TiN (60 nm) is reactively sputtered from a Ti target using two Kaufman IBSs, and will be referred to in this article as IBS_TiN. The primary IBS is used for sputtering from Ti target employing Ar and N₂ plasma, while the secondary

IBS is used for substrate bombardment with ions from pure N_2 plasma. Au is also deposited using primary IBS, to a thickness of 60 nm. NiCr (60 nm) was prepared by the same primary IBS, using pure Ar. IrO_x was obtained via DC reactive magnetron sputtering in an Ar/ O_2 plasma (100 nm) according to previous published methods [18]. PEDOT:PSS (PH1000 formulation from Clevis, plus 5 wt% ethylene glycol, 0.1 wt% 4-dodecylbenzenesulfonic acid and 1 wt% (3-glycidyloxypropyl)trimethoxysilane) was spin-coated at 3000 rpm and annealed for 1 h at 130 °C (giving roughly 100 nm thickness as measured by stylus profilometry). As a reference, we characterize commercial TiN used in multielectrode arrays (Multichannel Systems GmbH). These films are about 600 nm thick. To distinguish this TiN from our in-house prepared samples, we will refer to it as MCS_TiN.

2.2. Electrochemical cell

A homemade custom electrochemical cell allowed correct positioning and characterization of the electrodes under investigation. The cell was made from clear 5 mm thick acrylic sheets and a microscope glass slide as a front window. The internal volume of the cell was 9.3 ml. Microscope slides with deposited model stimulation electrodes were cut to (1×1) inch² pieces and horizontally inserted through a tight opening on the side of the cell. Polydimethylsiloxane was used to fix and seal the sample in position and to prevent any electrolyte leakage. The exposed area of each electrode was masked using a 70 μ m thick polyvinylchloride foil (Minitronic elektronik GmbH). The circular opening in the foil had a diameter of 3 mm, defining the electrode under test area (active electrode area = 0.0706 cm²). The cell was equipped with a Pt wire coil as counter (active area ~ 7 cm²) and an Ag/AgCl as reference electrodes, two openings provided access for the O_2 or H_2O_2 sensor and a teflon tube for O_2/N_2 purging. The sensor was placed in vicinity of the exposed active electrode material (distance = 200 μ m). The counter electrode is roughly 5 mm away from this area, at the top of the cell. Care should be taken that this distance is sufficient to ensure that any eventual products on the counter electrode do not affect the measurement. The cell was mounted on a submicrometer-precision XYZ stage (ThorLabs). Using a digital microscope (Q-SCOPE 20200-P), the sensor tip was positioned using XYZ stage to the point of light contact in the middle of the sample and then moved to the 200 μ m distance in the Z direction (figures 1(b) and S1). The cyclic voltammetry (CV) electrochemical characterization was carried out in a larger cell (from Redox.me) using an electrochemical active area of 1 cm², in a three-electrode configuration having Ag/AgCl as reference electrode and Pt wire as counter electrode in a range of potentials using 0.1 M phosphate buffer saline (PBS) solution as electrolyte.

2.3. Electrochemical measurements—DC and AC conditions

CV and chronoamperometry (DC conditions) were applied using an Ivium PocketSTAT2 potentiostat. For biphasic pulsing, a Digitimer DS4 biphasic constant current isolated stimulator was used, waveform was driven by a PicoScope 3404D oscilloscope with a built-in function generator. Transient voltages were recorded during biphasic pulsing by measuring voltage using the oscilloscope input (1 M Ω input impedance) between the electrode under test and an Ag/AgCl reference electrode. Data were collected in oxygenated and deoxygenated conditions. The relatively low input impedance is selected in order to provide a shunt resistance to prevent potential ratcheting and thus prevent the introduction of a DC bias offset voltage during AC pulsing experiments.

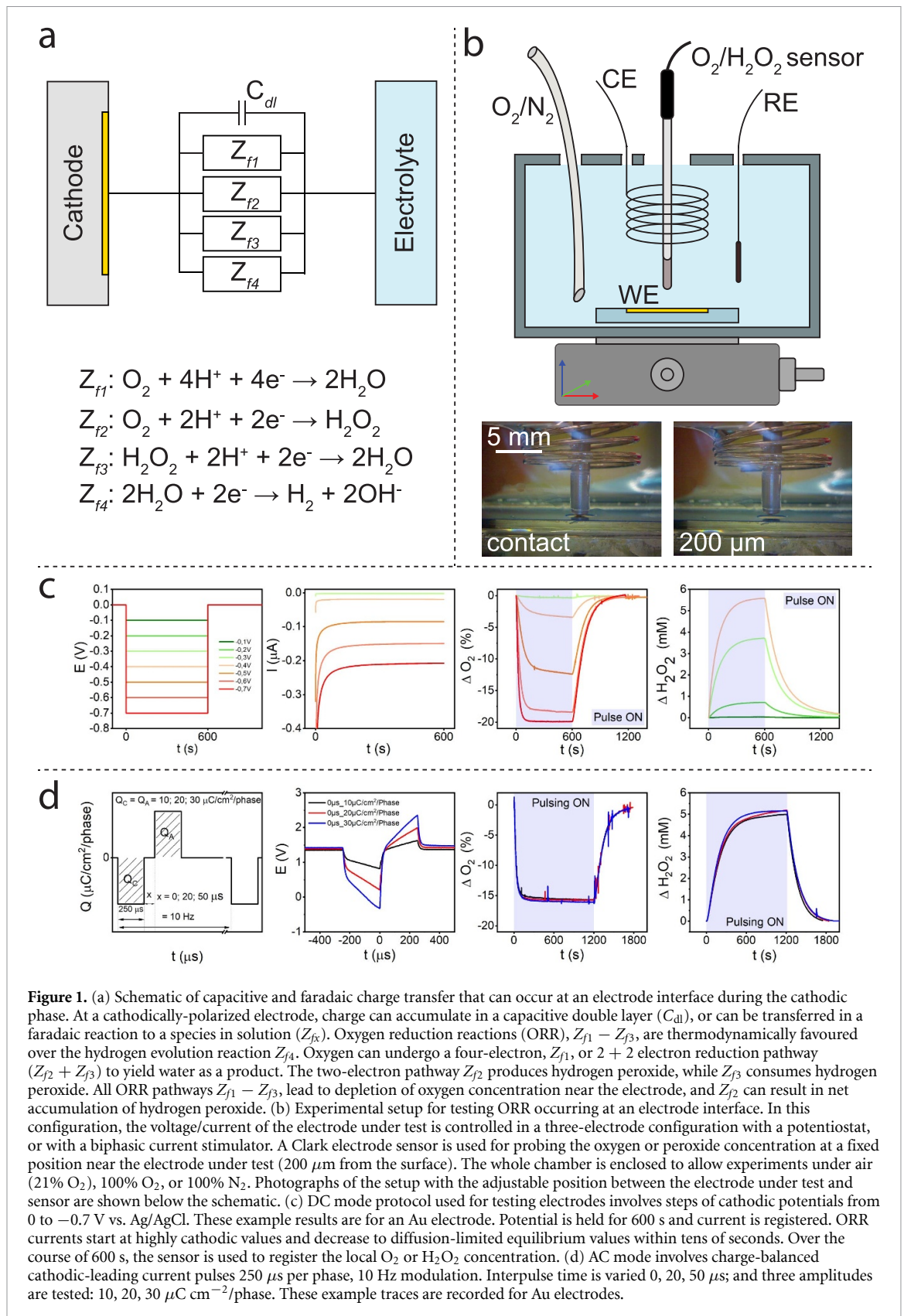
2.4. Clark electrode O_2 and H_2O_2 quantification

Local oxygen and peroxide concentrations were measured *in situ* during electrochemical measurements described above in section 2.2 using a four-channel microamperometric amplifier system (TBR4100, World Scientific Instruments), with four-channel analog-digital converter board (LabTrax, World Scientific Instruments). The respective sensor probes used were ISO-HPO-2 and ISO-OXY-2. The O_2 sensor was kept constantly polarized at a bias of 700 mV, meanwhile the H_2O_2 specific sensor at 450 mV. The sensors were always calibrated before the measurement of an individual material following the procedure reported in the instruction manual. The drop in O_2 concentration or increase in H_2O_2 was tracked by LabScribe software (World Scientific Instruments). It should be noted that the O_2 sensor functions along the classic Clark-electrode mechanism where oxygen is reduced at the sensing electrode, and oxygen reaches the sensor via an oxygen-permeable membrane. The peroxide sensor, on the other hand, operates via the oxidation of H_2O_2 , and is therefore also cross-sensitive to dissolved H_2 (via the H_2 oxidation reaction). For experiments where cathodic polarization of the electrode under test results in H_2 evolution, the sensor signal can register a false positive H_2O_2 signal. Caution should therefore be taken to test electrodes in deoxygenated electrolytes to establish the cathodic water-splitting onset. Peroxide sensor readings should only be accepted within the range before cathodic water splitting begins.

2.5. Finite element analysis of ORR at stimulation electrodes

Simulation of oxygen and peroxide diffusion was conducted with finite element method, implemented in COMSOL 5.5 software package and transport of diluted species module (www.comsol.com/product-download).

The experimental setup was reproduced within an axisymmetric 2D model. After the revolution, the



computational model obtained a cylindrical shape filled with water-based electrolytes (figure 5(a1)). Faradaic reactions occur on the area of a cathodic pixel located on the bottom. The diameter of pixel $d = 3 \text{ mm}$ was adopted from the experiment. The

water electrolyte domain spreads on 5 mm from the stimulation electrode, thus making the diameter of the electrolyte cylinder 13 mm and its height 5 mm (figure 5(a1)). The model contained two variables: c_{O_2} and $c_{H_2O_2}$, which goes for a concentration of dissolved

oxygen and hydrogen peroxide. Initial values were assigned as $c_{\text{O}_2}^{\text{saturated}} = 300 \mu\text{M}$ and $c_{\text{H}_2\text{O}_2} = 0 \mu\text{M}$.

We simulated both two- and four-electron reaction pathways separately. In case of two-electron case, we considered the possibility of further reduction of peroxide into water, or so called 2 + 2 reaction pathway. ORR was modelled via the introduction [19] of the empirical faradaic efficiency function (1), which modifies fluxes of oxygen and peroxide:

$$f_{\text{eff}} = f_1 + f_2 \frac{C_{\text{O}_2}^{\text{near pixel}}}{C_{\text{O}_2}^{\text{saturated}}}, \quad (1)$$

where $C_{\text{O}_2}^{\text{near pixel}}$ is oxygen concentration, measured at 10 nm from the stimulation electrode. The values of constants f_1 and f_2 range between 0 and 1 ($f_1 + f_2 = 1$) and depend on the type of cathode. If the constant f_2 is bigger than zero, the resulting flux of hydrogen peroxide will decrease with oxygen depletion.

The diffusion equations governed the change of oxygen and peroxide concentration

$$\frac{dc_i}{dt} + \nabla \cdot J_i = 0, \quad (2)$$

$$J_i = -D_i \nabla c_i, \quad (3)$$

where i goes for O_2 and H_2O_2 and J_i are fluxes of oxygen and peroxide. Diffusion coefficients at 23 °C are: $D_{\text{H}_2\text{O}_2} = 1.8 \times 10^{-9} \text{ m}^2 \text{ s}^{-1}$; $D_{\text{O}_2} = 2.5 \times 10^{-9} \text{ m}^2 \text{ s}^{-1}$ [20, 21].

Production and consumption of diluted O_2 and H_2O_2 molecules were carried out through boundary fluxes and can be found with all other boundary conditions in figure 5(a2). The model considered oxygen reduction into hydrogen peroxide in ratio 1:1 with a possible correction by faradaic efficiency function. Boundary fluxes R_{O_2} and $R_{\text{H}_2\text{O}_2}$ were defined as in the recent work of Abdullaeva *et al* [19]:

$$R_{\text{H}_2\text{O}_2} = \frac{FI}{2A} \times f_{\text{eff}}, \quad (4)$$

$$R_{\text{O}_2} = -\frac{FI}{2A} \times \left(f_{\text{eff}} + \frac{1 - f_{\text{eff}}}{2} \right), \quad (5)$$

where I is applied current (different in case of DC or AC simulations), F is Faraday constant, $A = 3.14 \times 1.5^2 \text{ mm}^2$ is the stimulation electrode area, f_{eff} is dimensionless faradaic efficiency function, defined by constants f_1 and f_2 and measured O_2 concentration $C_{\text{O}_2}^{\text{near pixel}}$ on the 10 nm distance from a production pixel.

In the case of the four-electron ORR reaction pathway, H_2O_2 does not participate in the process, and diffusion equations (2) and (3) is solved only for a concentration of oxygen with fluxes of O_2 molecules.

Assuming the absence of the reversed reaction, oxygen consumption is defined by

$$R_{\text{O}_2} = -\frac{FI}{4A}. \quad (6)$$

More details on the model construction can be found in the supplementary information appendix 1.

3. Results

3.1. CV characterization of electrodes

CV was used to characterize both capacitive charging and faradaic process occurring at each electrode material in PBS solution (figure 2). The system has been oxygenated and de-oxygenated (N_2 gas flow) to monitor the electrochemical behaviour of the materials under three different conditions (21% O_2 (atmospheric pressure), 100% N_2 and 100% O_2). Comparing CV curves from de-oxygenated conditions versus oxygenated ones can reveal which peaks are originating from ORR. The faradaic/capacitive charging behaviour differs markedly depending on the electrode material, nevertheless in all cases it is possible to observe an increase in cathodic current corresponding to oxygenation. ORR is apparent in CVs for voltages lower than +100 mV. For each material, we chose a smaller voltage window to measure in a region where capacitive charging dominates, allowing estimation of the double-layer capacitance of each electrode material (table 1; supplementary figure S2). CV scans for capacitance determination were obtained using a 1 mV step and current averaging according to methods described by Weltin and Kieninger [22].

3.2. DC chronoamperometry and direct measurements of ORR processes

While CV is useful to screen for possible ORR and other faradaic reactions, it does not reveal the magnitude of diffusion-limited oxygen reduction currents, or quantify the concentration of ORR products. To accomplish this, we combine DC chronoamperometry experiments with simultaneous recording of oxygen and hydrogen peroxide concentrations at a fixed point near the stimulation electrode surface (at a height of 200 μm). In these experiments, we measure current over time during the application of a constant potential (from +0.1 V to -0.9 V, by 0.1 V steps, depending on the material investigated) over a defined time (600 s) on each different stimulation electrode. The protocol and example results are plotted in figure 1(C). At potentials which are too anodic to reduce oxygen at a given electrode material, no sustained chronoamperometric currents are measurable. Once the onset potential is reached, sustained cathodic ORR current is clear. Onset potentials for ORR processes can be found in table 1. For reference,

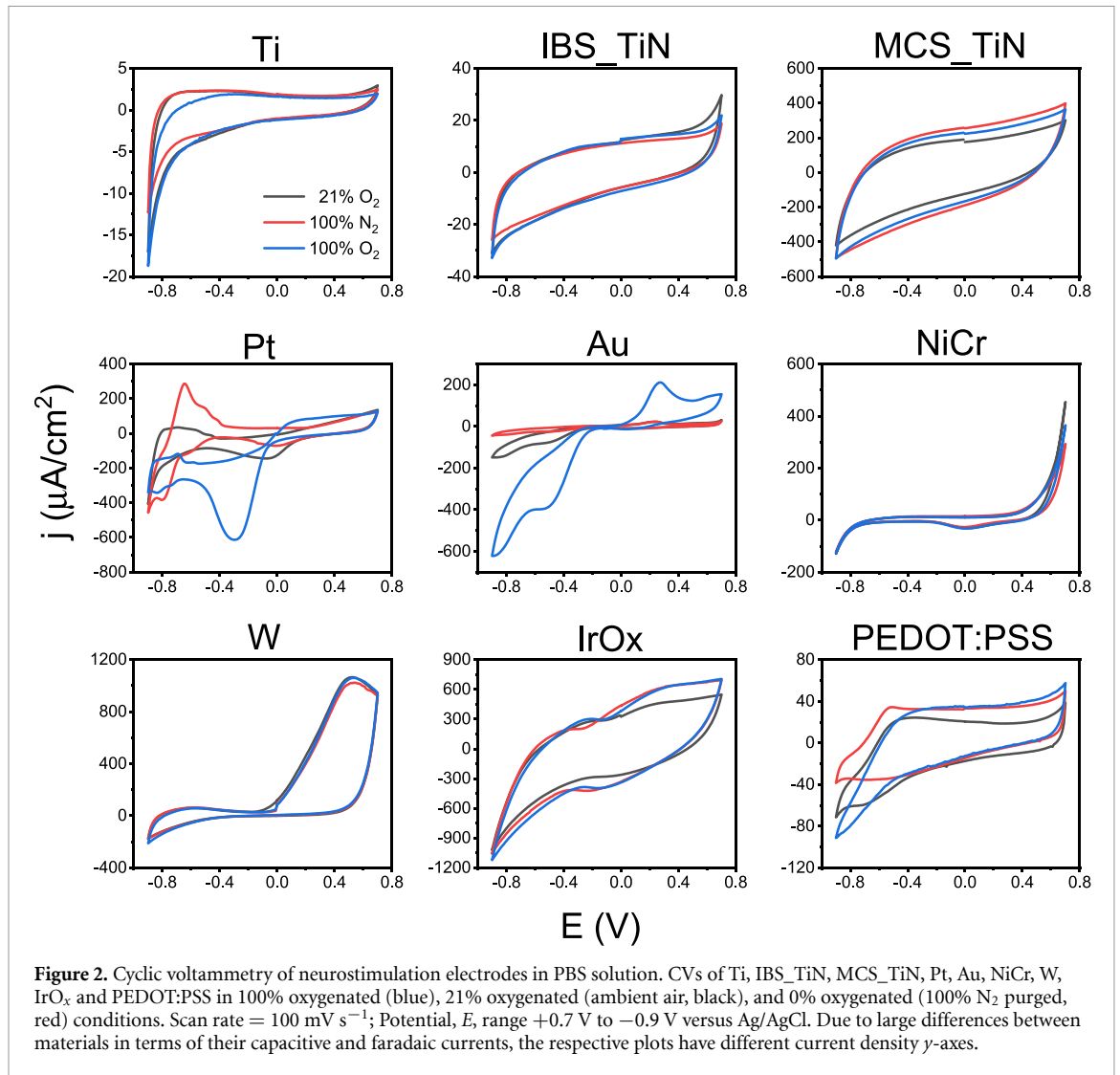


Table 1. ORR process onset potentials for each electrode materials in PBS solution, and electrochemical double-layer capacitance estimated for CVs measured in a nonfaradaic potential window (CVs shown in figure S2). Onset potentials for ORR and cathodic water-splitting are estimated from the chronoamperometry voltage-step profile and corresponding amperometric confirmation of oxygen reduction/peroxide generation. Potentials are given versus Ag/AgCl, [Cl⁻] = 0.12 M.

Material	Oxygen reduction onset (mV vs. Ag/AgCl)	Hydrogen peroxide evolution onset (mV vs. Ag/AgCl)	Hydrogen evolution reaction onset (mV vs. Ag/AgCl)	Double-layer capacitance (μF cm ⁻²)
Ti	-700	-700	-900	21
IBS_TiN	-500	-600	-1400	22
MCS_TiN	-500	-500	-1400	669
Pt	+100	0 ^a	-700	97
Au	-300	-300	-700	56
NiCr	-400	-400	-1000	24
W	-500	-600	-1000	69
IrO _x	0	0	-700	530
PEDOT:PSS	-600	-600	-1600	197

^a Only trace amounts of peroxide detected.

each sample is measured also in deoxygenated electrolyte to establish the cathodic onset potential for water splitting/H₂ evolution. These H₂ evolution onsets, also given in table 1, are always more negative than measured ORR potentials. Chronoamperometry

reveals a peak cathodic ORR current which then decays to a steady-state cathodic current. We define the steady-state current value as the current measured at the *t* = 600 s timepoint. The steady-state current as a function of applied potential for each material

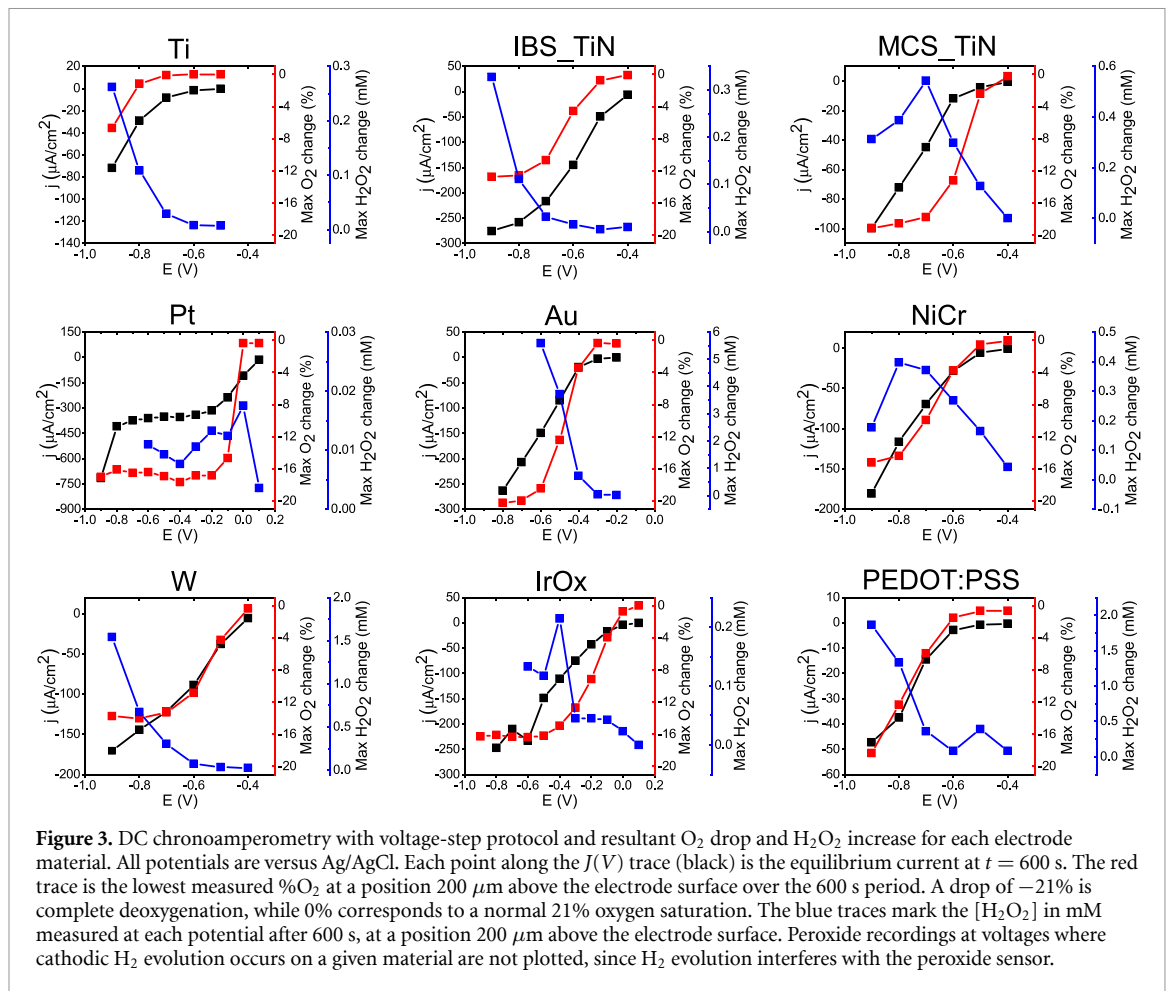
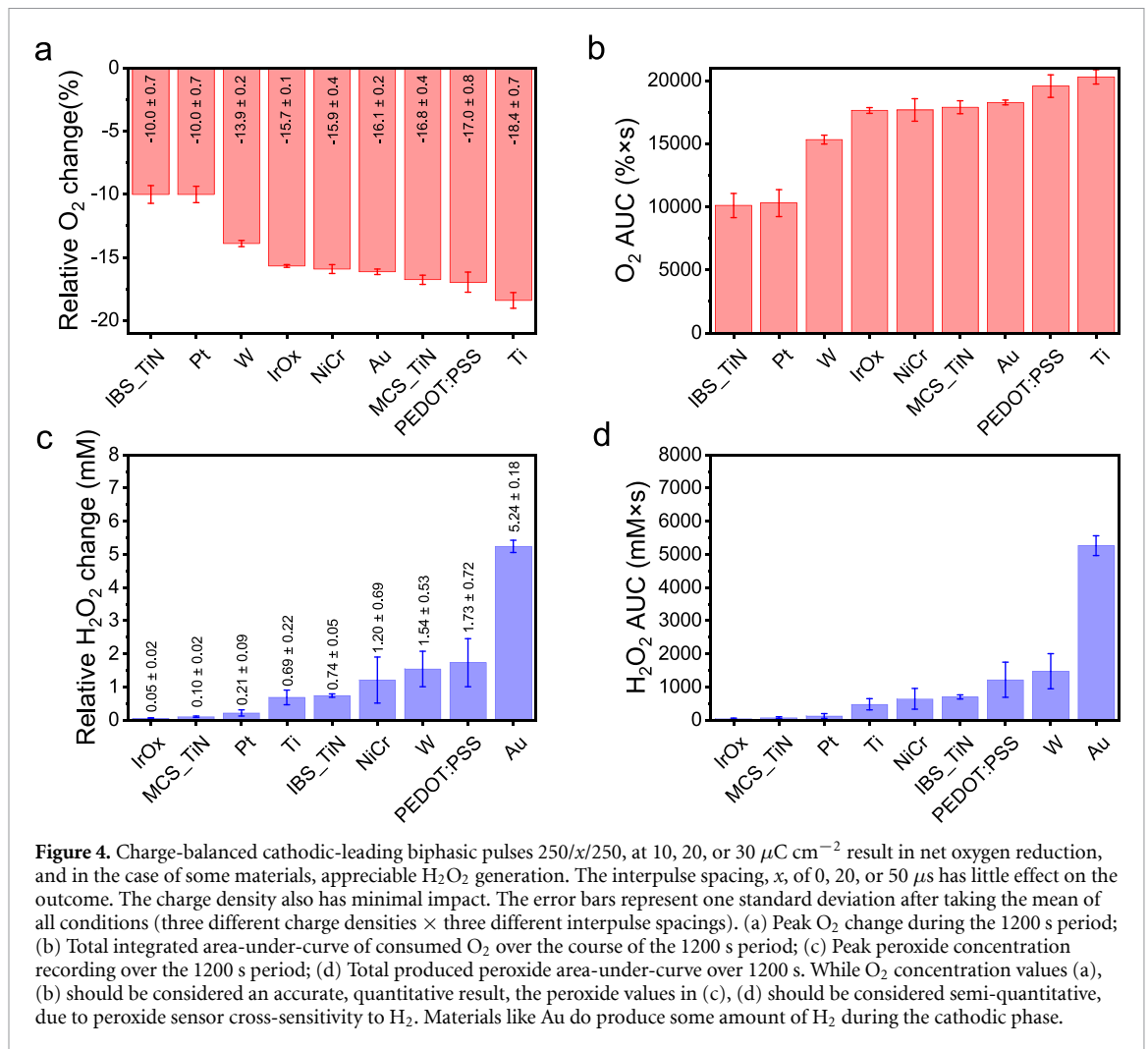


Figure 3. DC chronoamperometry with voltage-step protocol and resultant O_2 drop and H_2O_2 increase for each electrode material. All potentials are versus Ag/AgCl. Each point along the $J(V)$ trace (black) is the equilibrium current at $t = 600$ s. The red trace is the lowest measured $\%O_2$ at a position $200 \mu m$ above the electrode surface over the 600 s period. A drop of -21% is complete deoxygenation, while 0% corresponds to a normal 21% oxygen saturation. The blue traces mark the $[H_2O_2]$ in mM measured at each potential after 600 s, at a position $200 \mu m$ above the electrode surface. Peroxide recordings at voltages where cathodic H_2 evolution occurs on a given material are not plotted, since H_2 evolution interferes with the peroxide sensor.

is plotted in the black traces shown in figure 3. Simultaneously to recording chronoamperometry, the O_2/H_2O_2 amperometric sensor is active and recording the respective O_2 or H_2O_2 concentration value at a point in the electrolyte directly above the electrode-under-test. The measured values of O_2 or H_2O_2 concentration at the $t = 600$ s timepoint are shown in figure 3 as the red and blue traces, respectively. A change of -21% O_2 corresponds to a situation where the sensor records 0% oxygen, i.e. the calibrated lowest limit of a fully-deoxygenated solution. In between each voltage-step, the electrolyte in the cell is replaced with fresh, oxygenated electrolyte. It is noteworthy that all electrode materials can produce quite hypoxic conditions, with some such as Pt, Au, and PEDOT:PSS reaching nearly complete deoxygenation at higher cathodic potentials. The materials differ in their ability to produce peroxide from ORR. Au and PEDOT:PSS, for instance, produce concentrations into the millimolar range, while Pt generates barely-detectable trace amounts of peroxide. The recorded chronoamperometric currents and accompanying oxygen and peroxide measurements used to construct the plots in figure 3 can be found in supplementary figures S3–S11.

3.3. Direct measurements of ORR processes during AC stimulation protocols

Using the same configuration for amperometric sensing of oxygen and peroxide, we next applied charge balanced cathodic-leading pulses to the electrodes under test. The pulse duration per phase of charge balanced cathodic leading pulses used during experiments is kept constant ($250 \mu s$) and the interpulse spacing is changed to have three different durations (0 , 20 , or $50 \mu s$). We use a period of 100 ms ($f = 10$ Hz). We tested three charge density values: 10 , 20 , or $30 \mu C cm^{-2}/phase$. The total time for each AC experiment is 1200 s, compared with the DC chronoamperometry which was 600 s. This AC stimulation protocol and accompanying examples of measured amperometric transients are given in figure 1(d). The raw data of the amperometric traces of oxygen and peroxide over the course of AC pulsing are shown in figures S3–S11. In all cases, charge-balanced biphasic pulses led to drops in oxygen concentration comparable in magnitude to those found under the most cathodic DC conditions. The generation of peroxide as a byproduct varied based on material, with IrO_x and Pt producing only trace quantities, and Au and PEDOT:PSS producing the most. Surprisingly,



the magnitude of the charge density applied in the pulse had little effect on the peak and total amounts of ORR observed. The interpulse spacing has a minimal contribution on the overall change in $\% \text{O}_2$ or H_2O_2 concentration. Since both pulse amplitude and interpulse have no definitive impact on ORR levels, the data presented in figure 4 feature the nine different AC conditions all pooled to give a mean for a given material, with the standard deviation between conditions expressed by the error bar. Oxygen depletion and peroxide generation are expressed by both peak values, as well as the area-under-curve (AUC), the integral of the measured amperometric signal over time (1200 s) signifying the total amount of oxygen reduced/peroxide generated. During biphasic current pulses, voltage transients were collected (figure S12).

4. Discussion

4.1. ORR on electrode materials during CV and DC measurements

In this study, we have decided to investigate ORRs on commonly-used neurostimulation electrode materials, aiming to find out to what extent these reactions affect concentrations of dissolved oxygen and

hydrogen peroxide near the electrode. We selected eight representative electrode materials which we fabricated in thin-film form. Additionally, as a ninth material we studied a commercial TiN sample with high charge-injection capacity. The logic behind this study was to first measure CV in oxygenated versus deoxygenated electrolytes. This kind of characterization unambiguously reveals the presence of ORR. Next, we performed step-voltage chronoamperometric measurements to establish the magnitude of equilibrium ORR current density that is possible at a given electrode material. During the chronoamperometric measurements, O_2 or H_2O_2 concentration is registered in real time in the solution above the electrode surface. The magnitude of ORR currents, as well as the onset potentials, varied greatly between the samples, which is why the current density y -axes plotted in figures 2 and 3 are all different. These differences originate because of the electrocatalytic properties of each material with respect to ORR. Measured peroxide concentrations in this study varied over four orders of magnitude, from 1 μM to 10 mM. The use of a Clark-type chronoamperometric detection system is, to the best of our knowledge, the only method to measure peroxide concentrations over such a large

range. Optical methods based on photo- or fluorometric detection of dyes can be highly sensitive at low concentrations $<1 \mu\text{M}$ but these methods do not have a high dynamic range.

Firstly, we can turn our attention to results for platinum. Aside from being commonly used in many stimulation devices, Pt is a well-known textbook example of a good ORR catalyst [23]. In the CV measurements (figure 2), onset of ORR current is clearly observable around $+100 \text{ mV}$. Under 100% and 21% oxygen conditions, a pronounced ORR peak is visible at negative potentials. In N_2 -purged conditions, these ORR peaks are absent, and the reduction peaks can be assigned to proton absorption and then, by potentials more negative than -700 mV , clear hydrogen evolution reaction. The hydrogen evolution at potentials of -700 mV or more is present in both oxygenated and deoxygenated conditions, though oxygenation removes the peaks from Pt-H formation due to competitive adsorption of oxygen on the Pt surface. From chronoamperometry measurements of Pt electrodes, the steady-state ORR current densities in the range from $+100$ to -700 mV are higher on platinum than any of the other studied materials. Between -300 and -700 mV , there is a constant current density of $-400 \mu\text{A cm}^{-2}$ which can be assigned as the equilibrium ORR level. Based on what is known about the electrocatalytic properties of Pt, this ORR current is almost exclusively four-electron reduction of oxygen to water. This is confirmed via the $\text{O}_2/\text{H}_2\text{O}_2$ sensor measurements. All applied potentials between -100 mV and -900 mV yield the same pronounced oxygen depletion of -17% (-21% corresponds to complete deoxygenation). In parallel, the peroxide sensor reveals relatively low concentrations of peroxide close to the detection limit, around $5 \mu\text{M}$. This corroborates Pt as an efficient four-electron catalyst, moreover, Pt is well-known to decompose peroxide by either further two-electron reduction to water, or catalysed disproportionation to oxygen and water. Therefore, it is not surprising that our measurement of net peroxide production at Pt electrodes is minimal (though not completely absent). Taken together, these results for DC chronoamperometry show that Pt is an efficient oxygen reduction catalyst, and produces little peroxide as a by-product.

Following along by ordering materials with respect to their ORR onset potential, the next to consider is IrO_x . ORR is apparent from both CV and chronoamperometry. ORR is obscured in CV measurements due to the very high capacitive charging currents, which exceed in magnitude the maximum faradaic ORR currents. We calculate a capacitance of $530 \mu\text{F cm}^{-2}$ for our IrO_x samples. This material is well-known as a pseudofaradaic material with high capacitance. However, in chronoamperometry, the onsets and magnitudes of ORR currents are clearly

resolved. Sustained ORR current (between 50 and $250 \mu\text{A cm}^{-2}$) is apparent from potentials $<0 \text{ V}$. ORR current densities are not as high as on Pt, and oxygen depletion does not reach -16% until -0.5 V is applied. The ORR process produces minimal amounts of peroxide, which is detectable from potentials $<0 \text{ V}$.

The next 'classic' material we considered was gold. While gold is rarely used as a stimulation electrode material directly, it is frequently used as an interconnect, or as an electrode material in biosensor devices. ORR onset is visible in CV and chronoamperometry at around -300 mV , and faradaic currents are similar in magnitude to IrO_x . Au is recognized as an electrocatalyst which, unlike Pt, favours the two-electron pathway to generate peroxide [13]. Our results confirm that ORR current on Au is primarily via the peroxide pathway. Already by -500 mV , 5 mM of peroxide are detectable. Au overall is the most efficient peroxide-producing electrode among those we have tested. The two-electron pathway also corresponds to efficient oxygen depletion. Voltages more negative than -600 mV led to -21% oxygen level, that is, oxygen concentration reaches the lowest measurable value. In total, Au can be described as the material leading to the most deoxygenation and highest generation of peroxide.

PEDOT:PSS is a conducting polymer formulation which has attracted great attention as a promising low-impedance, high charge injection capacity electrode coating [24]. The CV of PEDOT:PSS shows a characteristic large capacitive background, nevertheless comparison of oxygenated and deoxygenated electrolytes clearly resolves the presence of ORR currents at potentials lower than -600 mV . PEDOT:PSS is known to be a highly-selective two-electron oxygen reduction catalyst [25]. The course of chronoamperometric currents for PEDOT:PSS resembles gold, though total equilibrium ORR currents are over four times lower than gold. Peroxide is generated from -600 mV onwards, reaching values into the mM range. A recent study by Dijk *et al* compared reactive oxygen species (ROS) generation and possible long-term safety of PEDOT:PSS versus Au, and found that thick PEDOT:PSS coatings can account for larger capacitive charge injection and less overall ROS generation [16]. The results of our DC measurements appear to be consistent with those findings as well.

NiCr and W are both materials which are not used in biomedical applications but are popular in basic neuroscience research. They both have relatively low double-layer capacitance and afford ORR with an onset potential of -400 mV . Equilibrium ORR currents are moderate ($50\text{--}200 \mu\text{A cm}^{-2}$), thus between the values of Au and PEDOT:PSS. W results in the production of peroxide with concentrations up to 2 mM , while NiCr generates about an order of magnitude less peroxide than W. These two materials

therefore are less active ORR catalysts than Pt or Au, yet more faradaic than PEDOT:PSS.

The final category of electrode materials are Ti and TiN, relevant in both basic research and biomedical stimulation devices. These materials are relatively the least faradaic. ORR currents on these materials are lower than on the other electrodes, and onset potentials are more negative. In CV and DC experiments, Ti is the most inert in terms of ORR current magnitude. Two types of TiN were studied, our own in-house thin film IBS_TiN and the MCS_TiN. The IBS_TiN is overall more faradaic than MCS_TiN or Ti, however the faradaic potential onsets are more cathodic than other studied materials, and currents remain relatively low. These findings correspond with what has been reported for titanium-based materials [26], in that they are regarded as being relatively inert and capacitive in terms of charge injection mechanism.

4.2. ORR during AC biphasic charge injection

While ORR is evident on all materials during CV measurements and during voltage-step chronoamperometric protocols, it can be postulated that rapid charge-balanced biphasic pulses will minimize ORR in terms of net oxygen consumption or peroxide generation. Lack of net ORR would be expected based on the logic of charge-balanced biphasic pulses minimizing any irreversible charge transfer into physiological solution [6, 8]. Nevertheless, the findings shown in figure 4 with biphasic pulses of 10, 20, and 30 $\mu\text{C cm}^{-2}$ amplitude show that ORR occurs to an extent similar to DC conditions. Surprisingly, charge amplitude and interpulse spacing have little effect on ORR. The traces for oxygen and peroxide changes over the AC pulsing experiment follow different time courses on different materials (figures S3–S11). For this reason, in figure 4 we plot both peak values of O_2 and H_2O_2 concentration differences (figures 4(a) and (c), respectively), as well as the total area-under-curve (AUC), shown in figures 4(b) and (d). The AUC corresponds to the integral value of O_2 consumed or H_2O_2 generated over 1200 s (at the given point 200 μm away from the centre of the stimulation electrode), and therefore may be a more relevant metric than peak value when comparing different materials. This is particularly evident for materials like NiCr, where a rapid peak of peroxide concentration is followed by a decline, as the resultant peroxide is further decomposed to water.

From these biphasic experiments, the materials resulting in the least irreversible ORR are IBS_TiN, and Pt. The oxygen concentration drops as well as peroxide evolution magnitudes presented in figure 4 do not completely correlate with expectations from CV and DC measurements for different electrode materials. In the case of Au and PEDOT:PSS, the results from biphasic pulses do correspond to expectations from DC measurements in that these two materials generate the most hydrogen peroxide and

also result in electrochemical deoxygenation to a high extent. IrO_x and Pt generate only trace amounts of peroxide. A material showing significant divergence from DC measurements is Ti: under biphasic pulsing, Ti leads to more deoxygenation than any other material. We do not have a clear mechanistic explanation for this result, and can speculate that this must have to do with oxygen consumption occurring during the anodic phase, likely during the anodization of the Ti surface and the reversible formation of an oxide layer which results in decrease of dissolved oxygen near the electrode. Another interesting comparison is between the two TiN samples. The porous MCS_TiN has 30 times higher double-layer capacitance than our in-house planar IBS_TiN sample. The MCS_TiN sample is known to have high capacitance due to a porous structure [17]. In both DC and AC conditions, the MCS_TiN sample is more active in ORR, consuming more oxygen. This indicates that the higher surface area affords also more active surface for faradaic reactions. As a point of reference to typical stimulation electrode characterization, we have recorded voltage transients for all AC conditions (figure S12). Such voltage transient data does not reveal ORR effects directly. The contributions of ORR can be interrogated by comparing transients for oxygenated versus deoxygenated electrolyte (figure S13). For most materials, the contribution of ORR as a charge-injection pathway is hinted by the apparent shift of the open circuit potential. Interpreting voltage transient data alone may give only limited information about the extent of ORR, which only becomes fully clear with the direct amperometric methods we have demonstrated. What can be emphasized from our findings is that electrochemical ORR during biphasic pulses is not as fully reversible as often assumed in the literature. Moreover, we have tried anodic-leading pulses, and found this also has little impact on total ORR. The overall characterization shows that all the electrode materials reduce O_2 in both AC and DC conditions. It should be noted that some of the peroxide data from AC pulsing may not be accurate due to sensor cross-sensitivity to H_2 . For most of the materials studied this is apparently not an issue, but Au electrodes do produce some H_2 during cathodic pulsing and therefore the resulting sensor signal is mixed, and not quantitative. The possibility for over-estimation also becomes apparent in the upcoming theoretical calculation section, where it is possible to calculate the range of concentrations which can be expected based on the amount of available oxygen.

5. Theoretical modelling

As we have shown experimentally, when ORR occurs at a neurostimulation electrode surface, oxygen is consumed and often peroxide accumulates. It is evident that gradients of $[\text{O}_2]$ and $[\text{H}_2\text{O}_2]$ form and evolve over time. To visualize these gradients, we have

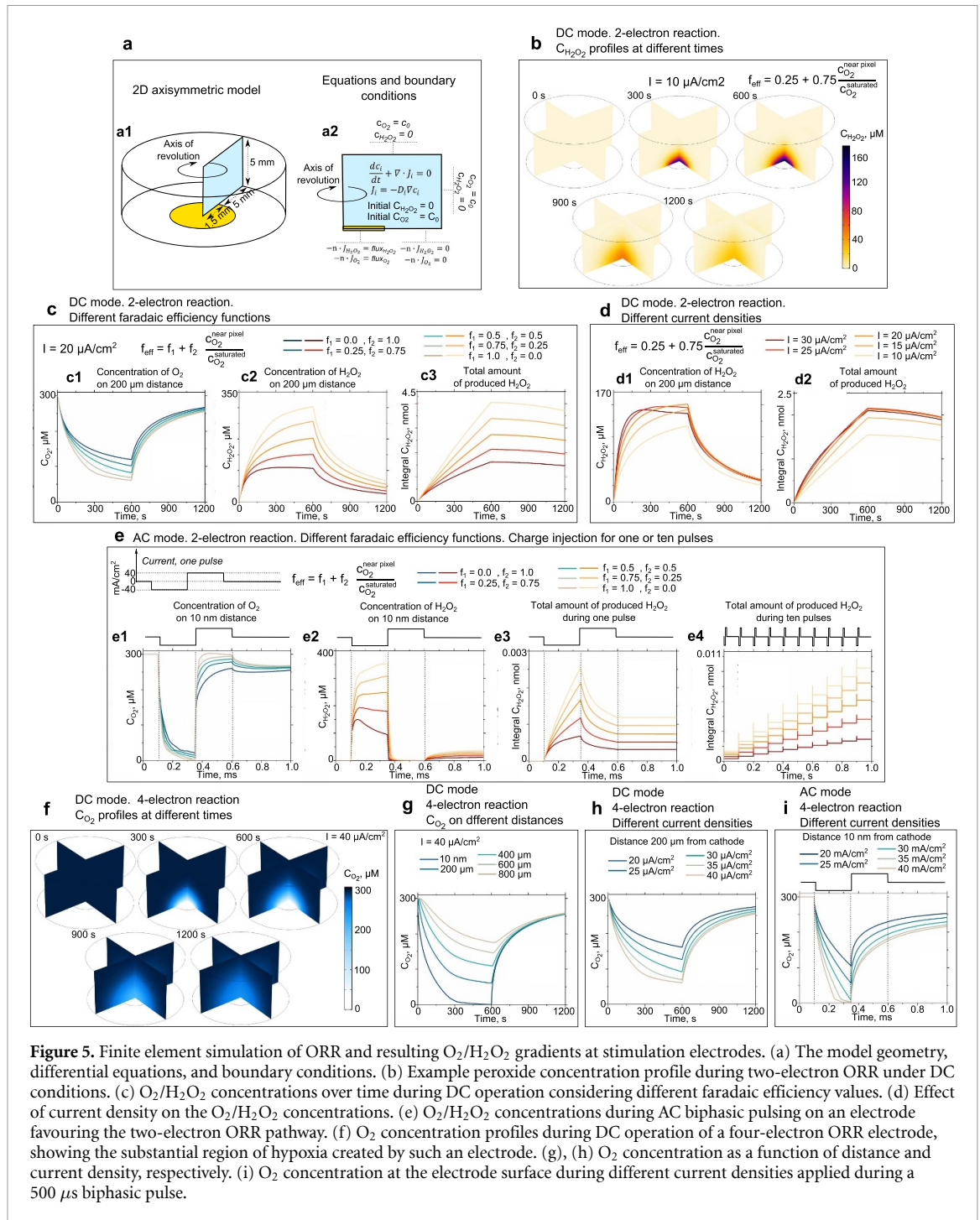


Figure 5. Finite element simulation of ORR and resulting O_2/H_2O_2 gradients at stimulation electrodes. (a) The model geometry, differential equations, and boundary conditions. (b) Example peroxide concentration profile during two-electron ORR under DC conditions. (c) O_2/H_2O_2 concentrations over time during DC operation considering different faradaic efficiency values. (d) Effect of current density on the O_2/H_2O_2 concentrations. (e) O_2/H_2O_2 concentrations during AC biphasic pulsing on an electrode favouring the two-electron ORR pathway. (f) O_2 concentration profiles during DC operation of a four-electron ORR electrode, showing the substantial region of hypoxia created by such an electrode. (g), (h) O_2 concentration as a function of distance and current density, respectively. (i) O_2 concentration at the electrode surface during different current densities applied during a 500 μs biphasic pulse.

performed a finite element simulation conducted in the COMSOL 5.5 software package. The finite element method is a good choice for this task because of its ability to reproduce the experimental setup in its actual sizes and flexibility in choosing the governing differential equation. We choose a two-dimensional axisymmetric model. After the revolution, it obtained a shape of a cylinder filled with electrolyte and the stimulation electrode at its bottom (figure 5(a1)). Concentrations of dissolved oxygen and hydrogen peroxide were simulated with diffusion equations and production/consumption fluxes on the stimulation electrode area (figure 5(a2)).

Faradaic ORR depends mainly on applied current and oxygen availability in the vicinity of a stimulation electrode. At the beginning of the process, we can assume that there is no hydrogen peroxide in the system and the concentration of dissolved oxygen is uniform across the electrolyte and equal to $C_{O_2}^{\text{saturated}} = 300 \mu\text{M}$. The stationary concentration of dissolved oxygen in the electrolyte depends on many factors, such as salinity or temperature. It can vary in the range between 250 and 450 μM . The value of $C_{O_2}^{\text{saturated}}$ affects simulation results quantitatively but does not change them qualitatively. While ORR happens, oxygen near the cathodically-polarized surface

is rapidly consumed while the reaction products diffuse away from the electrode. As was shown experimentally, preferable reaction pathways can be chosen by varying cathode material. For instance, platinum is known to be an efficient four-electron oxygen reduction electrocatalyst, meanwhile PEDOT:PSS or Au catalyse two-electron peroxide production. Simulations were carried out for two- and four-electron reaction pathways separately. In the case of two-electron reaction pathway, there was a possibility of an additional two-electron reduction of produced peroxide into water ($2 + 2$ reaction). The amount of current that goes to H_2O_2 reduction in $2 + 2$ -electron reaction, was defined with a faradaic efficiency according to equation (1) and fluxes according to equations (4) and (5).

Applying these calculations allows one to input realistic conditions used in a given neurostimulation experiment. Likewise, we wanted to use the model to understand the main differences between DC and AC faradaic production. An example of DC two-electron ORR with hydrogen peroxide as product can be found in figure 5(b), where $c_{\text{H}_2\text{O}_2}$ is depicted on two slices at different times up to 1200 s. A concentration gradient of H_2O_2 increases during the first 600 s. Because of the circular shape of the cathodic electrode, most of the produced peroxide is diffusing in a direction perpendicular to the stimulation electrode in a semi-spherical shape. The local $c_{\text{H}_2\text{O}_2}$ in front of the electrode centre will be higher than on its sides. Dissipation of produced H_2O_2 happens through the fixed concentration $c_{\text{H}_2\text{O}_2} = 0$ on the borders of electrolyte domain during the following 600 s, when no current is applied. In figures 5(c1) and (c2) one can find concentration profiles of c_{O_2} , $c_{\text{H}_2\text{O}_2}$ on the distance of $200 \mu\text{m}$ (as is in the experimental measurements) and in figure 5(c3) $\int c_{\text{H}_2\text{O}_2} dV$, which corresponds to the total amount of peroxide in nmoles, available in the system at a given time. Different values f_1 and f_2 define how efficiently the cathode can reduce O_2 into H_2O_2 . The shape of concentration profiles recorded on $200 \mu\text{m}$ can be significantly altered by changing f_1 and f_2 in a range from 0 to 1. If peroxide production is not efficient at low oxygen content ($f_1 = 0$, $f_2 = 1$), a sensor will record a clear ‘plateau’ in H_2O_2 concentration accompanied by lower deoxygenation. In the opposite case, if production efficiency of H_2O_2 is maximum ($f_1 = 1$, $f_2 = 0$) regardless of $C_{\text{O}_2}^{\text{near pixel}}$, H_2O_2 concentration, recorded by the sensor will have a steady increase in the form of ‘hill’ until the end of 600 s with strong deoxygenation. Despite the sublinear behaviour of H_2O_2 concentration profile in figure 5(c2), the total amount of produced H_2O_2 increases linearly with time and slowly dissipates through the boundaries in the following 600 s. This means that concentration data measured by the sensor cannot quantify the total amount of produced H_2O_2 in the system.

Faradaic efficiency is not the only factor affecting the shape of H_2O_2 concentration recorded by the sensor. An increase of the current density, applied to cathodic electrode from 10 to $30 \mu\text{A cm}^{-2}$ leads to the transition from the ‘hill’ shape towards ‘plateau’ and even further into ‘reversed hill’ at $30 \mu\text{A cm}^{-2}$ when recorded $c_{\text{H}_2\text{O}_2}$ decreases with time (figure 5(d1)). Considering the total amount of produced H_2O_2 , the system reaches its production limit at some current density, when additional increase of current density to the production pixel cannot increase peroxide content (figure 5(d2)). Production limit means that diffusional inflow of oxygen into the production zone is insufficient to support more ORR flux. This production limit can be surpassed in two cases: the temperature of electrolyte must be significantly increased (affecting the O_2 diffusion coefficient), or $C_{\text{O}_2}^{\text{saturated}}$ would have to be higher (oxygen-enriched electrolytes). All three simulated archetypes of H_2O_2 concentration profiles (‘hill’, ‘plateau’, ‘reversed hill’) and transition between them were indeed observed experimentally and can be found in figures S3–S9.

AC peroxide production is based on different processes compared to DC production. According to the traditional expectations of charge-balanced biphasic pulsing, one can anticipate an absence of H_2O_2 , because of compensation of all produced peroxide by the reversed reaction. Experiments show net H_2O_2 efflux from the cathodic electrode surface. To explain this effect, we performed calculations of ORR during one and ten AC pulses, summarized in figure 5(e). One AC pulse consists of three phases: forward $250 \mu\text{s}$ pulse, reversed $250 \mu\text{s}$ pulse, and 99 ms relaxation phase. It is essential to underline that current density, applied to the cathodic stimulation electrode in AC case ($\geq 40 \text{ mA cm}^{-2}$) is orders of magnitude larger than in the DC case ($\geq 10 \mu\text{A cm}^{-2}$). This means that the process which takes seconds in the DC case and occurs in milliseconds in the AC case. It is apparent in figures 5(e1) and (e2), where almost all oxygen near the production zone is consumed during the first $250 \mu\text{s}$ forward pulse, regardless of the faradaic efficiency. The concentration of H_2O_2 near the production zone also reaches large numbers. In case of maximized production (assuming all O_2 is reduced into H_2O_2), the recorded $c_{\text{H}_2\text{O}_2} \approx 350 \mu\text{M}$ can even surpass $C_{\text{O}_2}^{\text{saturated}} = 300 \mu\text{M}$. This fact is explained by the difference in diffusion coefficients of O_2 and H_2O_2 —oxygen inflow occurs faster than outflow of peroxide. After the forward pulse, the reverse pulse starts. It is reasonable to assume that the faradaic yield for H_2O_2 oxidation back to O_2 is close to unity. Therefore, H_2O_2 located near the cathode zone is oxidized into oxygen. $c_{\text{H}_2\text{O}_2}$ immediately drops to zero and c_{O_2} regains its initial value. While in figures 5(e1) and (e2) it may look as if all H_2O_2 is consumed during the reverse pulse, approximately half of

the total H_2O_2 produced during the AC pulse remains in the system (figure 5(e3)). This is due to diffusion. During the forward pulse, there is a flux of peroxide from the production zone. An additional gradient direction opens during the reversed pulse: towards the production zone with further consumption, while the gradient from the production zone remains. At this moment, there is a wave of peroxide near the stimulation electrode, which diffuses in two opposite directions, where the concentration of peroxide is zero. The duration of the reversed pulse is too low to reoxidize all the produced peroxide. At the same time, O_2 concentration is recovered not only by the consumption of peroxide but also by the diffusion of O_2 from the deeper electrolyte medium. After the reversed pulse, a relaxation stage occurs, where for more than 99 ms there is no current in the system. During this phase, H_2O_2 diffuses uniformly around all available space (resulting in a minor increase of $c_{\text{H}_2\text{O}_2}$ near production zone) and c_{O_2} decreases to compensate losses in electrolyte medium. At the end of the relaxation phase, the system almost recovers into its initial stage. Simulation of the sequential ten AC pulses shows a linear step-like increase of total H_2O_2 amount with each pulse figure 5(e4). The simulation shows that while DC conditions operate at small current values and thus a relatively slow reaction at the cathode goes for minutes, AC biphasic conditions result in rapid consumption of all available O_2 near the production zone at each current pulse and net oxygen depletion and, dependent on faradaic efficiency, peroxide accumulation.

The 2-electron reaction pathway implies the production of peroxide, and is to a lesser or greater degree present on all electrode materials tested in our work. However, some materials like Pt and IrO_x produce only trace amounts of peroxide, consistent with the expectation that they catalyse four-electron oxygen reduction to water. Four-electron reaction leads only to deoxygenation of electrolyte around the stimulation electrode. The electron multiplicity of the reaction translates to larger current requirements for the reaction, meaning twice slower consumption of dissolved oxygen at the same current density than during two-electron reaction. Oxygen concentration slices formed during DC faradaic production at a different time from 0 s to 1200 s can be found in figure 5(f). Oxygen is reduced with the formation of an apparent reversed gradient from the cathode zone. An oxygen-free region is formed at some distance from it, where all of the dissolved oxygen is consumed. A depletion of oxygen is observed at up to several mm from the pixel. Precise values of O_2 concentrations at a distance from 10 nm to 800 μm from the cathode are in plotted in figure 5(g). While four-electron reaction takes place, full deoxygenation is observed at 10 nm. However, at the distance of 200 μm , the simulation shows noticeable c_{O_2} presence. This effect is a manifestation of gradient formation because of the diffusion of O_2

from the electrolyte medium towards the production zone and explains the impossibility of detecting full deoxygenation at 200 μm experimentally. Gradual increase of current density from 20 to 40 $\mu\text{A cm}^{-2}$ allows recording of slow saturation of c_{O_2} towards its minimal value at the distance of 200 μm with the formation of a clear plateau (figure 5(h)). As for the AC case, similarly to the hydrogen peroxide production, the forward pulse almost immediately deoxygenates the whole cathodic zone on tens of nm deep (figure 5(i)). Assuming the absence of the reversed reaction, slow redistribution of oxygen starts after the cathodic phase, similar to the AC hydrogen peroxide production (figure 5(e1)).

6. Conclusions

Thermodynamically, oxygen is the most favourable electron acceptor present in physiological environments [22]. The formal potential of four-electron ORR to water as the product is 1.23 V more positive than the hydrogen evolution reaction. The formal potential of two-electron ORR to H_2O_2 is 0.7 V more positive than hydrogen evolution. However, this value is often cited misleadingly, as it is important to remember that formal potential assumes standard conditions, i.e. $[\text{H}_2\text{O}_2] = 1 \text{ M}$. Under physiological conditions, peroxide evolution is even more favourable since starting equilibrium concentrations of hydrogen peroxide are orders of magnitude lower than 1 M. By applying the Nernst equation, the actual thermodynamic potential for peroxide evolution is approx. 1.2 V, therefore as favourable as four-electron reduction [27]. Despite this likelihood of ORR happening at neurostimulation electrodes, the effects of ORR have not been extensively studied. The work we have done was aimed at introducing a set of methods for directly probing oxygen and peroxide concentrations at different neurostimulation electrodes. Using amperometric sensor measurements of oxygen and hydrogen peroxide concentration in the vicinity of electrodes we can unambiguously conclude that ORR occurs at all the studied materials, and that charge-balanced biphasic pulsing still leads to irreversible ORR. The method we present can in principle be applied *in vivo* by using appropriate microelectrodes which are commercially available.

Our results imply that during certain neuromodulation procedures, ORR may have consequences. Conditions near the electrode surface become hypoxic, which may significantly affect neuronal viability. Just a few minutes of hypoxia can trigger irreversible neuronal cell death [28, 29]. Many electrode materials additionally foster the accumulation of hydrogen peroxide. Hydrogen peroxide can be toxic at higher concentrations, and at lower concentrations functions as a signalling molecule in numerous pathways [30]. From the point of view of disturbing the balance of physiological oxygen the least, we can conclude

that IrO_x, Pt, and TiN appear to be the most promising. This applies to our in-house fabricated samples and depending on morphology and surface catalytic properties, results may vary significantly. An interesting observation is that the porous commercial TiN appears to be more active with respect to ORR than our planar thin film TiN. Therefore, just increasing double-layer capacitance of a sample does not necessarily minimize irreversible faradaic charge injection. Several of the other studied materials emerge as possibly problematic in neurostimulation applications due to relatively large hydrogen peroxide production: Au, W, and PEDOT:PSS can yield local peroxide concentrations in the mM range. All three materials are well-known to be active electrocatalysts for two-electron ORR, therefore our findings are not surprising. Extracellular peroxide concentrations in the range of 0.1–1 mM are toxic to cells [31]. More moderate concentrations in the range of tens of micromolar [H₂O₂] can have distinct electrophysiologic effects. Concentrations in this range cause oxidative modification of certain K_v7.x channels, which result in significantly higher outward potassium currents (the so-called M-current) and by this mechanism peroxide downregulates cellular excitability [19, 32]. On the other hand, cells expressing transient receptor vanilloid voltage-gated channels can be depolarized by the presence of such peroxide concentrations, therefore peroxide may cause action potential firing [33]. Our results for the different ORR behaviours occurring on different electrode materials can serve as a guide to eliminating problematic variables from electrophysiology experiments. Our findings of hypoxia being produced by DC currents, on the other hand, may be useful for electrically-addressable on-demand hypoxia or ROS delivery, which can be a useful experimental technique.

Data availability statement

All data that support the findings of this study are included within the article (and any supplementary files).

Acknowledgments

This project has been supported by funding from the European Research Council (ERC) under the European Union's Horizon 2020 research and innovation program (E D G Grant Agreement No. 949191), and a contribution from the city council of Brno, Czech Republic. The work was also supported by the Grant Agency of the Czech Republic under Contract 20-30129Y. Sample fabrication was supported by *CzechNanoLab Research Infrastructure* financed by MEYS CR (LM2018110). The computations were performed on resources provided by the Swedish National Infrastructure for Computing (SNIC) at NSC and HPC2N.

Author contributions


E D G conceived the project. J E designed and built the measurement setup. J E; L M; and M N performed all electrochemical experiments. I S developed the finite element model and did all calculations. M N set up the AC pulsing experiments and wrote software for data collection. J E and L M performed all data analysis. J B and I G fabricated all electrodes, except for IrO_x, which was fabricated by X T V and S I. E D G supervised the project. The paper was written by all co-authors.

Conflict of interest

The authors declare no competing financial interests.

ORCID iDs

Jiří Ehlich  <https://orcid.org/0000-0003-0478-6875>

Ihor Sahalianov  <https://orcid.org/0000-0002-0609-471X>

Imrich Gablech  <https://orcid.org/0000-0003-4218-1287>

Xuan Thang Vu  <https://orcid.org/0000-0001-6797-2443>

Sven Ingebrandt  <https://orcid.org/0000-0002-0405-2727>

Eric Daniel Głowacki  <https://orcid.org/0000-0002-0280-8017>

References

- [1] Lozano A M *et al* 2019 Deep brain stimulation: current challenges and future directions *Nat. Rev. Neurol.* **15** 148–60
- [2] Kwan H, Garzoni L, Liu H L, Cao M, Desrochers A, Fecteau G, Burns P and Frasch M G 2016 Vagus nerve stimulation for treatment of inflammation: systematic review of animal models and clinical studies *Bioelectron. Med.* **3** 1–6
- [3] Cameron T 2004 Safety and efficacy of spinal cord stimulation for the treatment of chronic pain: a 20-year literature review *J. Neurosurg.* **100** 254–67
- [4] Krames E S, Peckham P H and Rezaei A R 2009 *Neuromodulation* (London: Academic)
- [5] Grill W M and Kirsch R F 2000 Neuroprosthetic applications of electrical stimulation *Assist. Technol.* **12** 6–20
- [6] Cogan S F 2008 Neural stimulation and recording electrodes *Annu. Rev. Biomed. Eng.* **10** 275–309
- [7] Merrill D R, Bikson M and Jefferys J G R 2005 Electrical stimulation of excitable tissue: design of efficacious and safe protocols *J. Neurosci. Methods* **141** 171–98
- [8] Merrill D R 2010 The electrochemistry of charge injection at the electrode/tissue interface *Implantable Neural Prostheses 2* eds D D Zhou and E Greenbaum (New York: Springer) pp 85–138
- [9] Günter C, Delbeke J and Ortiz-Catalan M 2019 Safety of long-term electrical peripheral nerve stimulation: review of the state of the art *J. Neuroeng. Rehabil.* **16** 13
- [10] Leung R T, Shivdasani M N, Nayagam D A X and Shepherd R K 2015 *In vivo* and *in vitro* comparison of the charge injection capacity of platinum macroelectrodes *IEEE Trans. Biomed. Eng.* **62** 849–57
- [11] Boehler C, Carli S, Fadiga L, Stieglitz T and Asplund M 2020 Tutorial: guidelines for standardized performance tests for electrodes intended for neural interfaces and bioelectronics *Nat. Protocols* **15** 3557–78

- [12] Shepherd R K, Carter P, Dalrymple A, Enke Y L, Wise A K, Nguyen T, Firth J, Thompson A and Fallon J B 2021 Platinum dissolution and tissue response following long-term electrical stimulation at high charge densities *J. Neural Eng.* **18** 036021
- [13] Morton S L, Daroux M and Mortimer J T 1991 The role of oxygen reduction in electrical stimulation of nervous tissue *Proc. Annual Conf. Engineering in Medicine and Biology Society* vol 13 pp 552–3
- [14] Cogan S F, Ehrlich J, Plante T D, Gingerich M D and Shire D B 2010 Contribution of oxygen reduction to charge injection on platinum and sputtered iridium oxide neural stimulation electrodes *IEEE Trans. Biomed. Eng.* **57** 2313–21
- [15] Musa S, Rand D R, Bartic C, Eberle W, Nuttin B and Borghs G 2011 Coulometric detection of irreversible electrochemical reactions occurring at Pt microelectrodes used for neural stimulation *Anal. Chem.* **83** 4012–22
- [16] Dijk G, Ruijgrok H J and Connor R P O 2021 PEDOT:PSS-coated stimulation electrodes attenuate irreversible electrochemical events and reduce cell electropermeabilization *Adv. Mater. Interfaces* **8** 2100214
- [17] Egert U, Schlosshauer B, Fennrich S, Nisch W, Fejtl M, Knott T, Müller T and Hämmerle H 1998 A novel organotypic long-term culture of the rat hippocampus on substrate-integrated multielectrode arrays *Brain Res. Protocols* **2** 229–42
- [18] van Ooyen A, Topalov G, Ganske G, Mokwa W and Schnakenberg U 2009 Iridium oxide deposited by pulsed dc-sputtering for stimulation electrodes *J. Micromech. Microeng.* **19** 074009
- [19] Abdullaeva O S, Sahalianov I, Ejneby M S, Jakešová M, Zozoulenko I, Liin S I and Glowacki E D 2022 Faradaic pixels for precise hydrogen peroxide delivery to control M-type voltage-gated potassium channels *Adv. Sci.* **9** 2103132
- [20] Wise D L and Houghton G 1966 The diffusion coefficients of ten slightly soluble gases in water at 10–60 °C *Chem. Eng. Sci.* **21** 999–1010
- [21] van Stroey-Beizen S A M M, Everaerts F M, Janssen L J J and Tacke R A 1993 Diffusion coefficients of oxygen, hydrogen peroxide and glucose in a hydrogel *Anal. Chim. Acta* **273** 553–60
- [22] Weltin A and Kieninger J 2021 Electrochemical methods for neural interface electrodes *J. Neural Eng.* **18** 052001
- [23] Song C and Zhang J 2008 Electrocatalytic Oxygen Reduction Reaction *PEM Fuel Cell Electrocatalysts and Catalyst Layers: Fundamentals and Applications* ed J Zhang (London: Springer) pp 89–134
- [24] Donahue M J, Sanchez-Sanchez A, Inal S, Qu J, Owens R M, Mecerreyes D, Malliaras G G and Martin D C 2020 Tailoring PEDOT properties for applications in bioelectronics *Mater. Sci. Eng. R* **140** 100546
- [25] Mitra E et al 2019 Electrocatalytic production of hydrogen peroxide with Poly(3,4-ethylenedioxythiophene) electrodes *Adv. Sustain. Syst.* **3** 1800110
- [26] Schaldach M, Hubmann M, Weigl A and Hardt R 1990 Sputter-deposited TiN electrode coatings for superior sensing and pacing performance *Pacing Clin. Electrophysiol.* **13** 1891–5
- [27] Katsounaros I, Schneider W B, Meier J C, Benedikt U, Biedermann P U, Auer A A and Mayrhofer K J J 2012 Hydrogen peroxide electrochemistry on platinum: towards understanding the oxygen reduction reaction mechanism *Phys. Chem. Chem. Phys.* **14** 7384
- [28] Kirino T 2000 Delayed neuronal death *Neuropathology* **20** 95–7
- [29] Lipton P 1999 Ischemic cell death in brain neurons *Physiol. Rev.* **79** 1431–568
- [30] Sies H and Jones D P 2020 Reactive oxygen species (ROS) as pleiotropic physiological signalling agents *Nat. Rev. Mol. Cell Biol.* **21** 363–83
- [31] Sies H 2017 Hydrogen peroxide as a central redox signaling molecule in physiological oxidative stress: oxidative eustress *Redox Biol.* **11** 613–9
- [32] Gamper N, Zaika O, Li Y, Martin P, Hernandez C C, Perez M R, Wang A Y C, Jaffe D B and Shapiro M S 2006 Oxidative modification of M-type K⁺ channels as a mechanism of cytoprotective neuronal silencing *EMBO J.* **25** 4996–5004
- [33] Lodola F, Rosti V, Tullii G, Desii A, Tapella L, Catarsi P, Lim D, Moccia F and Antognazza M R 2019 Conjugated polymers optically regulate the fate of endothelial colony-forming cells *Sci. Adv.* **5** eaav4620